

Enhanced reversibility and unusual microstructure of a phase-transforming material

Yintao Song^{1*}, Xian Chen^{1*}, Vivekanand Dabade¹, Thomas W. Shield¹ & Richard D. James¹

Materials undergoing reversible solid-to-solid martensitic phase transformations are desirable for applications in medical sensors and actuators¹, eco-friendly refrigerators^{2,3} and energy conversion devices⁴. The ability to pass back and forth through the phase transformation many times without degradation of properties (termed ‘reversibility’) is critical for these applications. Materials tuned to satisfy a certain geometric compatibility condition have been shown^{2,5–14} to exhibit high reversibility, measured by low hysteresis and small migration of transformation temperature under cycling^{6,9,12,15}. Recently, stronger compatibility conditions called the ‘cofactor conditions’^{5,15} have been proposed theoretically to achieve even better reversibility. Here we report the enhanced reversibility and unusual microstructure of the first martensitic material, $\text{Zn}_{45}\text{Au}_{30}\text{Cu}_{25}$, that closely satisfies the cofactor conditions. We observe four striking properties of this material. (1) Despite a transformation strain of 8%, the transformation temperature shifts less than 0.5 °C after more than 16,000 thermal cycles. For comparison, the transformation temperature of the ubiquitous NiTi alloy shifts up to 20 °C in the first 20 cycles^{9,16}. (2) The hysteresis remains approximately 2 °C during this cycling. For comparison, the hysteresis of the NiTi alloy is up to 70 °C (refs 9, 12). (3) The alloy exhibits an unusual riverine microstructure of martensite not seen in other martensites. (4) Unlike that of typical polycrystal martensites, its microstructure changes drastically in consecutive transformation cycles, whereas macroscopic properties such as transformation temperature and latent heat are nearly reproducible. These results promise a concrete strategy for seeking ultra-reliable martensitic materials.

Martensitic transformations are diffusionless, solid-to-solid phase transformations characterized by a change of crystal structure^{8,14}. Accompanying this structural change, the mechanical (such as shape memory¹²), electromagnetic (such as magneto- and electro-caloric^{2,3,11}), and transport (such as conductivity¹⁷) properties of the material can also change abruptly, which is useful in practical applications. During cyclic phase transformation, the desired functionality of martensitic materials degrades^{2,9,16,18}. It is generally believed that the degradation of properties originates from the stressed transition layer between the two phases^{13,14,19}. The same transition layer gives rise to an energy barrier that causes thermal hysteresis⁷. During the martensitic phase transformation, the stress in the transition layer drives irreversible processes, such as the formation of dislocations and the nucleation of microcracks¹⁹. These irreversible processes in turn lead to functional degradation and failure. Hence, high functional stability (that is, reversibility) can be achieved by reducing or even eliminating the elastic transition layer, which leads to the study of the geometric compatibility of the two phases.

A successful strategy^{5–7,9,10,13} for eliminating this transition layer has been found by using the crystallographic theory of martensite^{13,14,20,21}. According to this theory, if certain mild conditions are satisfied, each pair of twinned variants (a ‘twin system’) can form a laminated microstructure that meets austenite at a low-elastic-energy transition layer. The

theory generically has four solutions per twin system, yielding four austenite–martensite interfaces, but corresponding to only two twinning volume fractions, f^* and $1 - f^*$. Figure 1a shows a typical solution of the crystallographic theory. The special cases $f^* = 0$ and $f^* = 1$ can occur and correspond to transition-layer-free interfaces between austenite and single variant martensite (Fig. 1b). This degeneracy occurs if and only if the condition $\lambda_2 = 1$ is satisfied¹³, where λ_2 is the middle eigenvalue of the 3×3 ‘transformation stretch matrix’ U , which is obtained from X-ray measurements of lattice parameters and knowledge of the space groups of the two phases^{8,14}. Thus, the strategy for elimination of the stressed transition layer is to make $\lambda_2 \rightarrow 1$ by systematically tuning the composition of alloys. This strategy has been successfully applied to shape memory alloys^{6,7,12}, magnetocaloric materials² and energy materials^{22,23}.

The cofactor conditions represent a further degeneracy of the crystallographic theory of martensite^{5,15}. The cofactor conditions are necessary and sufficient conditions on the lattice parameters and the twin system such that the crystallographic theory has solutions for every volume fraction $0 \leq f \leq 1$. This is in contrast with the above cases where there are only two volume fractions per twin system. When the cofactor conditions are satisfied, one can continuously vary the volume fraction of the twin variants while retaining the low-elastic-energy interface with austenite. The cofactor conditions consist of three sub-conditions that restrict the distortion and twin system. The first is $\lambda_2 = 1$. The second is $|U^{-1}\hat{e}| = 1$ for type I twins and $|U\hat{e}| = 1$ for type II twins, where \hat{e} is a unit vector aligned with the twofold axes associated to these twins. Here, types I and II refer to certain classic symmetry relations^{8,14} that hold for the lattices on each side of a twin plane. Physically, these conditions imply the presence of certain unstretched directions for the distortion and for the inverse distortion. The third is a mild condition that is only relevant for compound twins. A detailed description of these concepts is given in the Supplementary Information.

A detailed theoretical analysis¹⁵ of cofactor conditions, summarized also here in the Supplementary Information, yields further unexpected implications of cofactor conditions. First, if cofactor conditions are satisfied for a twin system, they are typically satisfied also by a large family of twin systems. Second, if the twin system is type I or type II⁸, half of these solutions of the crystallographic theory require no transition layer at all. These yield zero-elastic-energy interfaces with austenite for every volume fraction f . Finally, if cofactor conditions are satisfied simultaneously by twin systems of both types I and II, numerous further zero-elastic-energy microstructures can be constructed from triple junctions formed by austenite and a pair of type I twinned martensite variants (A and B in Fig. 1c, d), and quad junctions formed by four pairwise twinned variants (Fig. 1e, f). These two simple junctions can be combined to form the ‘riverine’ zero-elastic-energy microstructure seen in Fig. 1g. Figure 1c, e and g are drawn accurately using the measured lattice parameters of $\text{Zn}_{45}\text{Au}_{30}\text{Cu}_{25}$, but perturbed very slightly to satisfy the cofactor conditions exactly.

This plethora of zero-elastic-energy deformations implies that the material has a great many ways of accommodating non-transforming

¹Department of Aerospace Engineering and Mechanics, University of Minnesota, Minneapolis, Minnesota 55455, USA.

*These authors contributed equally to this work.

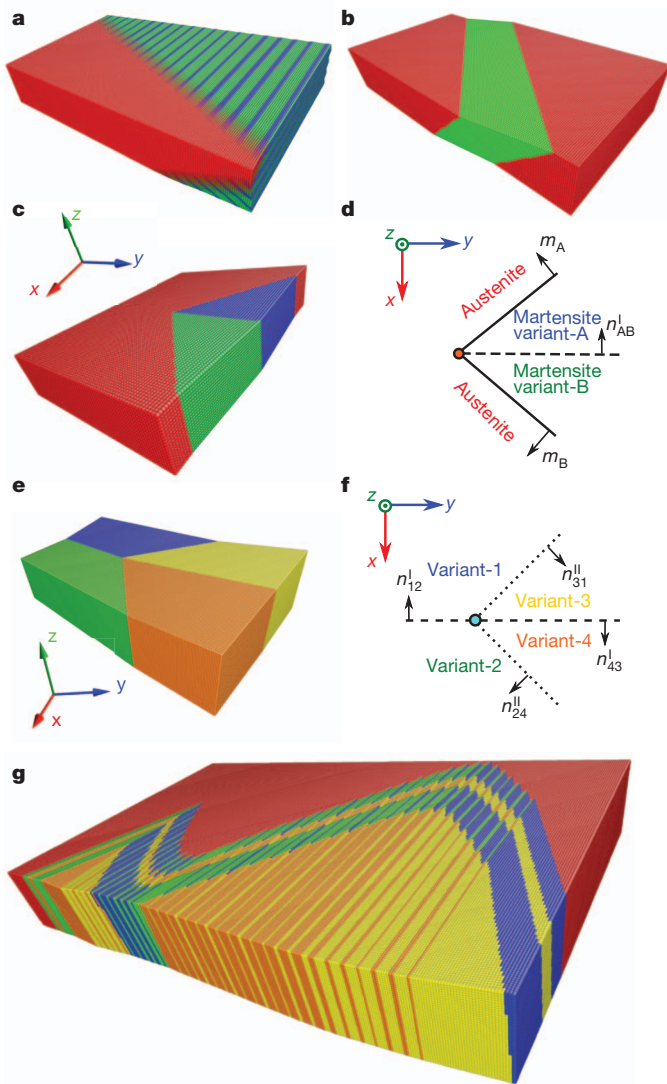


Figure 1 | Various austenite–martensite boundaries and special junctions. **a**, Planar phase boundary with transition layer. **b**, Planar phase boundary without transition layer. **c**, A triple junction formed by austenite and a type I twin pair, and its two-dimensional projection (**d**). **e**, A quad junction formed by four variants, and its two-dimensional projection (**f**). In **d** and **f**, solid lines are austenite–martensite interfaces with normals m_A and m_B , whereas dashed and dotted lines are type I and type II twin walls respectively, with normals given by n^I and n^{II} , with subscripts indicating the neighbouring variants. **g**, Curved phase boundary and riverine microstructure. In **a–c**, **e** and **g**, the red lattice represents austenite, and other colours are variants of martensite.

inclusions, defects and precipitates during transformation. The benefit of having such large classes of low-energy deformations is a recurring theme in the literature on phase transformations in polycrystals^{12,24}. The cofactor conditions combine the advantages for hysteresis of having no transition layer with the existence of a great many low-energy deformations and the implications for reversibility.

Literature values of lattice parameters^{25,26} suggested that the Heusler-type system Zn_2AuCu was a suitable candidate to tune so as to satisfy the cofactor conditions. We prepared a set of seven $Zn_{45}Au_xCu_{55-x}$ alloys in the composition range $20 \leq x \leq 30$ for preliminary study. After this preliminary screening, a set of three alloys, with $x = 25$ (Au25), $x = 27$ (Au27) and $x = 30$ (Au30) respectively, were prepared by arc-melting high-purity elements in vacuum. Their functional stability properties were characterized by X-ray diffraction and calorimetry (Supplementary Methods). For this alloy system, the austenite is face-centred cubic (L2₁ ordering)²⁵, whereas the martensite phase is

M18R monoclinic²⁶. Following the ‘recipe’ provided in the Supplementary Information, we use $X_I = |U^{-1}\hat{e}|$ and $X_{II} = |U\hat{e}|$ to quantify the cofactor conditions for twins of types I and II, respectively. The values $X_{I/II} = \lambda_2 = 1$ represents exact satisfaction of the cofactor conditions in each case. The values of λ_2 , X_I and X_{II} (Table 1) show that (1) all three samples have λ_2 close to 1, and Au30 is the closest; (2) by changing the composition from Au25 to Au30, both X_I and X_{II} approach 1 simultaneously, and both are closest to 1 in Au30. In theory, X_I and X_{II} need not approach 1 simultaneously. Thus, the coincidental satisfaction of the cofactor conditions for twins of both type I and type II is apparently an accident, or else arises for reasons that are currently unknown.

Thermal cycling was done by the combination of differential scanning calorimetry (DSC) and a thermal cycling apparatus designed by us involving a thin-film heater competing against a liquid-nitrogen-cooled sample holder (Supplementary Fig. 3). For each specimen DSC measurements were made for the first 64 cycles. For each of the subsequent 2^n DSC cycles (where $n = 7, 8, \dots$), the sample was removed from the cycling apparatus and a DSC measurement was made. The sample was then returned to the apparatus for further cycling. During cycling in the apparatus, the surface morphology of the specimen was observed *in situ* by optical microscopy.

The results of DSC measurements are shown in Fig. 2. Figure 2a–c shows the calorimetric curves of the DSC cycles. All three samples have sharp transformation peaks, from which the austenite start (A_s), austenite finish (A_f), martensite start (M_s) and martensite finish (M_f) temperatures are determined by the conventional onset-point construction. Hysteresis, calculated by $(A_s + A_f - M_s - M_f)/2$ for the first cycle, is given in Fig. 2a–c. The DSC curves clearly shift in Au25 and Au27, but no significant shift is observed in Au30. The data are summarized in Fig. 2d, which shows the shift of transformation temperatures versus the cycle number on a log scale. We see that the transformation temperatures migrate downwards significantly in Au25 and Au27, whereas in Au30, the transformation temperature oscillates slightly around the initial value. In Au25 the size of the hysteresis increases significantly with cycling, but the average transformation temperature migrates downward. These behaviours suggest that significant damage occurs in both phases due to the transformation process, but that the average free energy of martensite is more strongly increased. Also seen in Fig. 2a–c, and most clearly demonstrated by Au25, is that the area under the transformation peak, corresponding to the latent heat, shrinks during cycling. This is summarized in Fig. 2e. Again, as the composition is changed from Au25 to Au30, the shrinkage of latent heat decreases, and it almost disappears in Au30. We extended the cycling test on Au30 to $2^{14} = 16,384$ cycles. The shift of the transformation temperatures and the shrinkage of latent heat during this long test are plotted in Fig. 2f. We see only small changes of these values in Au30 even after such a large number of thermal cycles. This is remarkable given that Zn_2AuCu is a soft alloy with a relatively high homologous temperature (the transformation temperature to melting temperature ratio) of about 0.22. Taken together, these observations cast significant doubt on the standard explanations for hysteresis based on pinning of interfaces by defects or thermal activation.

Figure 3a, c and e shows the surface morphology of each specimen in the phase in which it was originally polished (austenite for Au30 and martensite for Au25 and Au27), after 64 cycles. Figure 3b, d and f shows the microstructure of the other phase in several consecutive

Table 1 | Geometric compatibility conditions in three specimens

	Au25	Au27	Au30
λ_2	1.0092 ± 0.0002	1.0086 ± 0.0001	1.0006 ± 0.0002
X_I	0.9899 ± 0.0034	1.0090 ± 0.0001	1.0081 ± 0.0008
	1.0179 ± 0.0028	1.0222 ± 0.0024	1.0339 ± 0.0005
X_{II}	1.0256 ± 0.0050	1.0056 ± 0.0007	0.9996 ± 0.0008
	0.9893 ± 0.0017	0.9884 ± 0.0005	0.9695 ± 0.0004

The reason that X_I and X_{II} have two values for each material is given in Supplementary Information III.

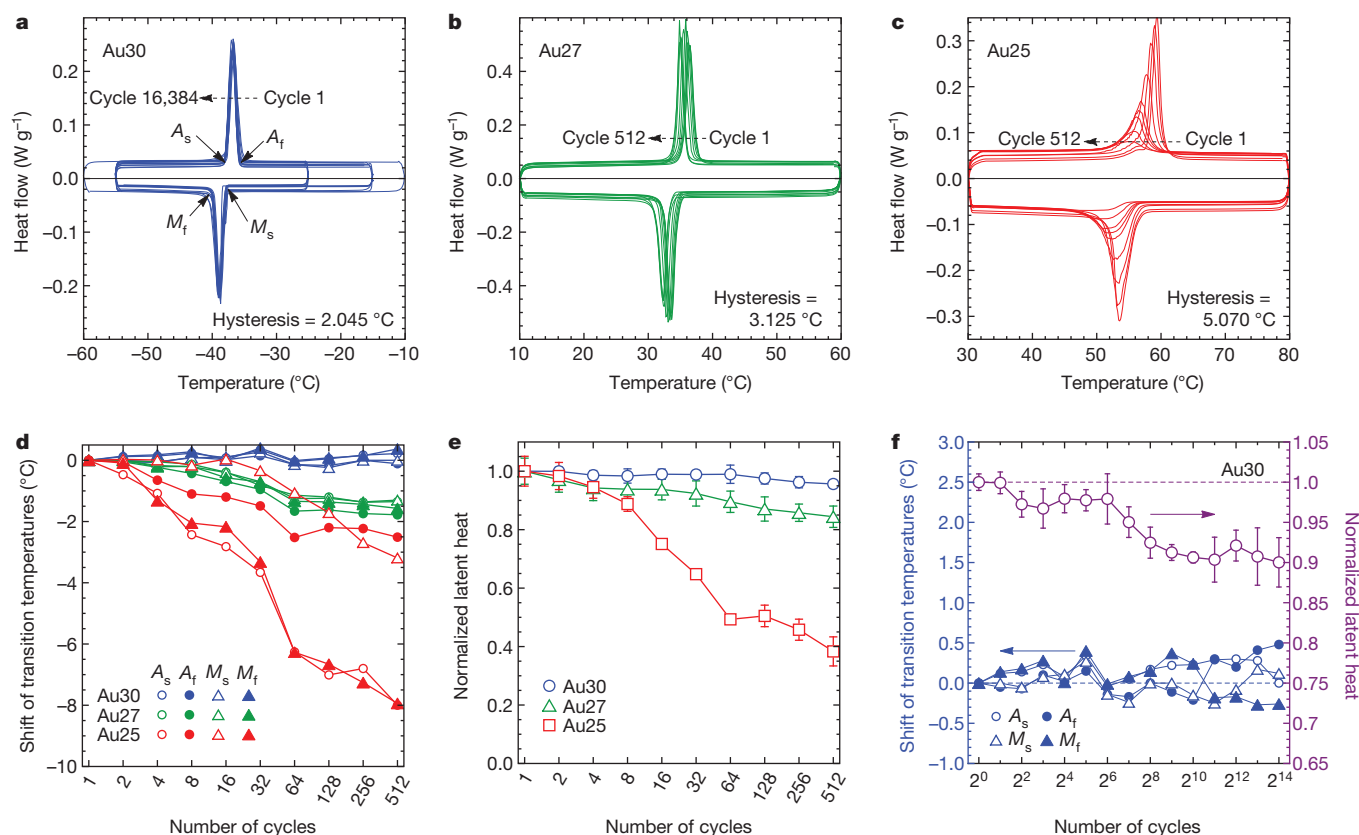


Figure 2 | Functional stability of $Au_xCu_{55-x}Zn_{45}$ alloys where $x = 25$ (Au25), $x = 27$ (Au27) and $x = 30$ (Au30) during thermal cycling. **a–c**, DSC data of three specimens. The values of hysteresis, $(A_s + A_f - M_s - M_f)/2$, are calculated for the virgin cycle. **d**, The shift of austenite start (A_s), finish (A_f) and martensite start (M_s), finish (M_f)

temperatures. **e**, Latent heat measured in different cycles normalized by the value of the virgin cycle. Data points represent the average values of latent heat upon heating and cooling, and the error bars represent the differences between them. **f**, Functional stability of Au30 extended to 2¹⁴ = 16,384 cycles.

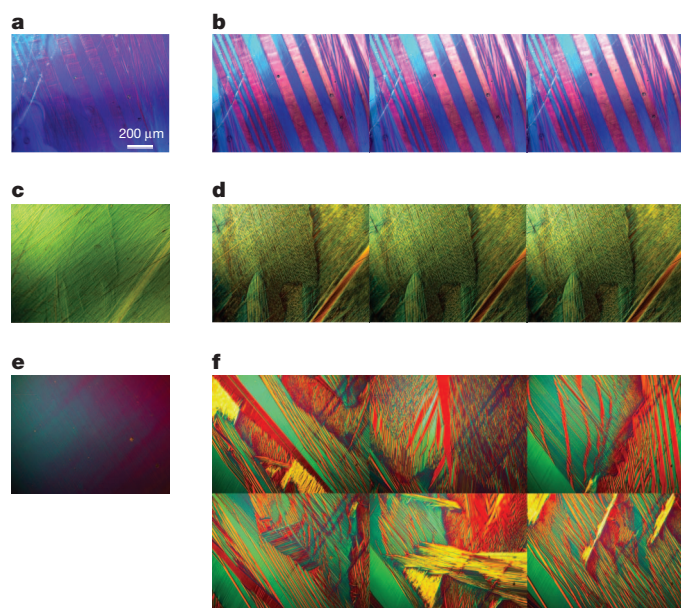


Figure 3 | Microstructures in consecutive cycles. **a**, Polished martensite surface of Au25 after 64 cycles. **b**, Austenite (inverse) microstructure of Au25 for three consecutive cycles immediately after taking the micrograph in **a**. **c**, Polished martensite surface of Au27 after 64 cycles. **d**, Austenite (inverse) microstructure of Au27 for three consecutive cycles immediately after taking the micrograph in **c**. **e**, Polished austenite surface of Au30 after 64 cycles. **f**, Martensite microstructure of Au30 for six consecutive cycles immediately after taking the micrograph in **e**.

cycles immediately following those of Fig. 3a, c and e. We see that Au25 and Au27 show the same microstructure in all three cycles. However, the microstructure in Au30 is completely different in each of the six cycles (see the Supplementary Video), which is repeated throughout the cycling process.

Figure 4 shows the morphology of Au30 in a single grain (about 1 mm), obtained by stitching a dozen micrographs together. We can see various hierarchical microstructures that resemble those predicted by the above theory. Particularly, the riverine microstructure shown on the left of Fig. 4, also seen frequently during cycling, has to our knowledge not been seen in any martensitic material. An enlarged view of the edge of this riverine microstructure is provided in Supplementary Fig. 4. In forthcoming work involving electron backscatter diffraction and transmission electron microscopy we will investigate the connection between Fig. 4 and theoretical predictions more precisely.

Of the three samples, Au30, which is the one that most closely satisfies cofactor conditions for both type I and type II twin systems, exhibits the lowest hysteresis and the highest functional stability. Also, its microstructure is completely unlike any other martensite we have seen. For example, the repeating microstructures upon phase transformation cycles in Au25 and Au27 are consistent with the common observation^{27–30} that polycrystal martensitic materials exhibit detailed reproducibility of microstructure and acoustic emission traces, related to ‘return-point memory’²⁸. Au30 clearly loses this memory. We conjecture that this observation is linked to the large number of ways of constructing low- and zero-elastic-energy austenite–martensite interfaces in materials satisfying the cofactor conditions. The vast number of low-energy states possible in this material implies that minor variations of conditions from cycle to cycle lead to diverse microstructures.

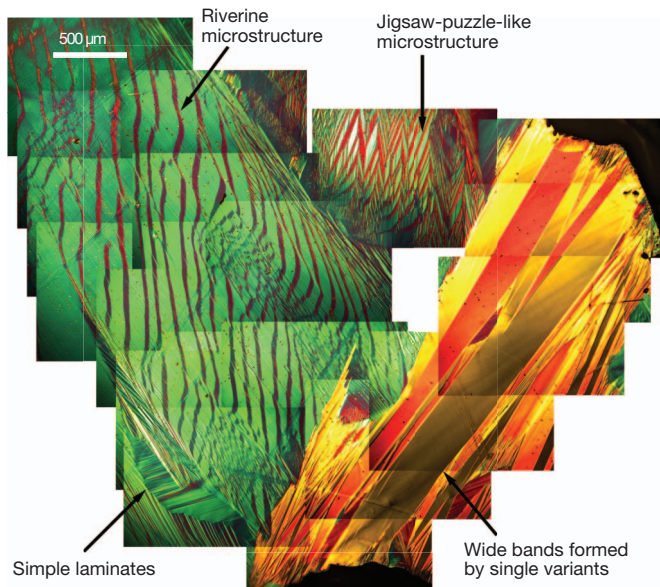


Figure 4 | Various hierarchical microstructures in Au₃₀, the alloy most closely satisfying the cofactor conditions for both type I and type II twin systems.

We have thus found the first martensitic material that closely satisfies the cofactor conditions, and it happens to satisfy them for both type I and type II twin systems. This material exhibits ultrahigh reversibility and unusual microstructure. The theory for its fabrication can readily be adapted to other alloy systems, because it depends only on lattice parameters that can be finely tuned by changing the composition. Our result suggests a universal strategy for developing ultra-reliable martensitic materials particularly suited to medical, microelectronic and energy applications.

METHODS SUMMARY

Polycrystal ingots with nominal composition $Au_xCu_{55-x}Zn_{45}$ ($x = 25, 27$ and 30) were prepared by melting Cu (99.9999%), Au (99.999%) and Zn (99.9999%) pellets in an evacuated (10^{-5} mbar) and sealed silica capsule. The capsule was kept in the furnace, the temperature of which was varied as follows: 600°C for 2 h, 800°C for 8 h and finally $1,200^\circ\text{C}$ for 24 h. To promote homogeneity, the ingots were again reheated to $1,200^\circ\text{C}$ for 24 h while the silica capsules were rotated about the axis of a tube furnace at 30 r.p.m. The net weight losses were less than 0.01%. Finally, the ingots were annealed at 650°C for 24 h and quenched in ice water.

A TA Q1000 machine calibrated by indium was used for DSC measurements at the rate of $\pm 10^\circ\text{C}$ per minute. Specimens were finely polished on both sides at the beginning to ensure good thermal contact. For each sample, the first two cycles were scanned from -100°C to 180°C to identify the transformation temperatures. The following DSC cycles were then scanned over a temperature range of about 50°C covering the identified transformation temperatures.

The cycling on the thermal stage that we designed was performed over a small temperature range determined by the stabilization of microstructure upon transformation, which was about 10°C . The cycling frequency was about 0.1 Hz. Microstructure was observed by optical microscopy with differential interference contrast technology. The colour code was not calibrated.

X-ray diffraction was done using a Bruker AXS microdiffractometer (Cu $K\alpha$ radiation source) with a temperature-controlled stage. Data was collected by general area detector diffraction system (GADDS). The sample surface was polished before being mounted to the stage at room temperature. The peak positions were refined using the JADE v7.0 software for the precise determination of lattice parameters.

Received 15 May; accepted 6 August 2013.

1. Walia, H., Brantley, W. A. & Gerstein, H. An initial investigation of the bending and torsional properties of Nitinol root canal files. *J. Endod.* **14**, 346–351 (1988).
2. Liu, J., Gottschall, T., Skokov, K. P., Moore, J. D. & Gutfleisch, M. O. Giant magnetocaloric effect driven by structural transitions. *Nature Mater.* **11**, 620–626 (2012).

3. Moya, X. *et al.* Giant electrocaloric strength in single-crystal BaTiO_3 . *Adv. Mater.* **25**, 1360–1365 (2013).
4. Srivastava, V., Song, Y., Bhatti, K. & James, R. D. The direct conversion of heat to electricity using multiferroic alloys. *Adv. Energy Mater.* **1**, 97–104 (2011).
5. James, R. D. & Zhang, Z. In *Magnetism and Structure in Functional Materials* (eds Planes, A., Mañosa, L. & Saxena, A.) 159–175 (Springer, 2005).
6. Cui, J. *et al.* Combinatorial search of thermoelastic shape-memory alloys with extremely small hysteresis width. *Nature Mater.* **5**, 286–290 (2006).
7. Zhang, Z., James, R. D. & Müller, S. Energy barriers and hysteresis in martensitic phase transformations. *Acta Mater.* **57**, 4332–4352 (2009).
8. Pitteri, M. & Zanzotto, G. *Continuum Models for Phase Transitions and Twinning in Crystals* (Chapman and Hall/CRC, 2010).
9. Zarnetta, R. *et al.* Identification of quaternary shape memory alloys with near-zero thermal hysteresis and unprecedented functional stability. *Adv. Funct. Mater.* **20**, 1917–1923 (2010).
10. Delville, R. *et al.* Transmission electron microscopy study of phase compatibility in low hysteresis shape memory alloys. *Phil. Mag.* **90**, 177–195 (2010).
11. Srivastava, V., Chen, X. & James, R. D. Hysteresis and unusual magnetic properties in the singular heusler alloy $\text{Ni}_{45}\text{Co}_5\text{Mn}_{40}\text{Sn}_{10}$. *Appl. Phys. Lett.* **97**, 014101 (2010).
12. Bechtold, C., Chluba, C., de Miranda, R. L. & Quandt, E. High cyclic stability of the elastocaloric effect in sputtered TiNiCu shape memory films. *Appl. Phys. Lett.* **101**, 091903 (2012).
13. Ball, J. M. & James, R. D. Fine phase mixtures as minimizers of energy. *Arch. Ration. Mech. Anal.* **100**, 13–52 (1987).
14. Bhattacharya, K. *Microstructure of Martensite: Why It Forms and How It Gives Rise to the Shape-Memory Effect* (Oxford Univ. Press, 2003).
15. Chen, X., Srivastava, V., Dabade, V. & James, R. D. Study of the cofactor conditions: conditions of supercompatibility between phases. *J. Mech. Phys. Solids* <http://dx.doi.org/10.1016/j.jmps.2013.08.004> (2013).
16. Tadaki, T., Nakata, Y. & Shimizu, K. Thermal cycling effects in an aged Ni-rich Ti-Ni shape memory alloy. *Trans. Jpn. Inst. Metals* **28**, 883–890 (1987).
17. Mott, N. F. *Metal-Insulator Transitions* Ch. 5 (Taylor & Francis, 1990).
18. Eggeler, G., Hornbogen, E., Yawny, A., Heckmann, A. & Wagner, M. Structural and functional fatigue of NiTi shape memory alloys. *Mater. Sci. Eng. A* **378**, 24–33 (2004).
19. Norfleet, D. M. *et al.* Transformation-induced plasticity during pseudoelastic deformation in Ni-Ti microcrystals. *Acta Mater.* **57**, 3549–3561 (2009).
20. Wechsler, M. S., Lieberman, D. S. & Read, T. A. On the theory of the formation of martensite. *J. Metall./Trans. AIME* **197**, 1503–1515 (1953).
21. Bowles, J. S. & Mackenzie, J. K. The crystallography of martensite transformations I/II. *Acta Metall.* **2**, 129–137 (1954).
22. Meethong, N., Huang, H.-Y., Speakman, S., Carter, W. & Chiang, Y.-M. Strain accommodation during phase transformations in olivine-based cathodes as a materials selection criterion for high-power rechargeable batteries. *Adv. Funct. Mater.* **17**, 1115–1123 (2007).
23. Louie, M. W., Kisilitsyn, M., Bhattacharya, K. & Haile, S. M. Phase transformation and hysteresis behavior in $\text{Cs}_{1-x}\text{Rb}_x\text{H}_2\text{PO}_4$. *Solid State Ion.* **181**, 173–179 (2010).
24. Bhattacharya, K. & Kohn, R. V. Symmetry, texture and the recoverable strain of shape-memory poly-crystals. *Acta Mater.* **44**, 529–542 (1996).
25. Tadaki, T., Okazaki, H., Yoshiyuki, N. & Shimizu, K. Atomic configuration determined by ALCHEMI and X-ray diffraction of the L_{21} type parent phase in a Cu-Au-Zn shape memory alloy. *Mater. Trans. JIM* **31**, 935–940 (1990).
26. Tadaki, T., Okazaki, H., Yoshiyuki, N. & Shimizu, K. Atomic configuration determined by ALCHEMI and X-ray diffraction of a stabilized M18R martensite in a β phase Cu-Au-Zn alloy. *Mater. Trans. JIM* **31**, 941–947 (1990).
27. Amengual, A. *et al.* Systematic study of the martensitic transformation in a Cu-Zn-Al alloy. Reversibility versus irreversibility via acoustic emission. *Thermochim. Acta* **116**, 195–208 (1987).
28. Sethna, J. P. *et al.* Hysteresis and hierarchies: dynamics of disorder-driven first-order phase transformations. *Phys. Rev. Lett.* **70**, 3347–3350 (1993).
29. Sethna, J. P., Dahmen, K. A. & Myers, C. R. Crackling noise. *Nature* **410**, 242–250 (2001).
30. Vives, E., Soto-Parra, D., Mañosa, L., Romero, R. & Planes, A. Imaging the dynamics of martensitic transitions using acoustic emission. *Phys. Rev. B* **84**, 060101 (2011).

Supplementary Information is available in the online version of the paper.

Acknowledgements We acknowledge the financial support of MURI projects FA9550-12-1-0458 (administered by AFOSR) and W911NF-07-1-0410 (administered by ARO). This research also benefited from the support of NSF-PIRE grant number OISE-0967140. Y.S. thanks the Graduate School of the University of Minnesota for support through a Doctoral Dissertation Fellowship.

Author Contributions R.D.J. is the Principal Investigator and initiated and supervised the work. Y.S. designed the thermal cycling apparatus and carried out optical and calorimetric experiments. X.C. performed X-ray diffraction measurements and theoretical calculations of microstructure. V.D. synthesized all the specimens used in the study. T.W.S. provided expertise in the experimental design and data acquisition. All authors discussed the results and approved the manuscript. Y.S., X.C. and R.D.J. interpreted the data and wrote the manuscript.

Author Information Reprints and permissions information is available at www.nature.com/reprints. The authors declare no competing financial interests. Readers are welcome to comment on the online version of the paper. Correspondence and requests for materials should be addressed to R.D.J. (james@umn.edu).